Physics of the Earth and Planetary Interiors 168 (2008) 37–48

Contents lists available at ScienceDirect

Physics of the Earth and Planetary Interiors

journal homepage: www.elsevier.com/locate/pepi

Three-dimensional tomography and rock properties of the Larderello-Travale geothermal area, Italy

R. De Matteis[a,*], T. Vanorio[b], A. Zollo[c], S. Ciuffi[d], A. Fiordelisi[d], E. Spinelli[d]

[a] Dipartimento di Studi Geologici ed Ambientali, Università del Sannio, Benevento, Italy
[b] Department of Geophysics, Stanford University, Stanford, CA, USA
[c] Dipartimento di Scienze Fisiche, Università di Napoli Federico II, Napoli, Italy
[d] ENEL GEM-Geothermal Production, Pisa, Italy

ARTICLE INFO

Article history:
Received 16 May 2007
Received in revised form 27 February 2008
Accepted 29 April 2008

Keywords:
P- and S-wave velocity
Seismic tomography images
Rock properties
Geothermal field

ABSTRACT

In a geothermal area, a detailed knowledge of the three-dimensional velocity structures aids the management of the field and the further development of the geothermal source. Here, we present a high-resolution study of the three-dimensional S-wave velocity structures from microearthquake travel times for the Larderello-Travale geothermal field, Italy. We have also deduced the V_p/V_s and $V_p \times V_s$ parameters for this area to emphasize the deep variations in the physical rock properties due to fluid content and porosity. Furthermore, effective porous medium modelling has been performed for site-relevant lithologies, to improve our interpretation of the results in terms of rock physics signatures. This has allowed us to estimate the variation range of the seismological parameters investigated, as well as their sensitivity for suitable rock under specific physical conditions. Low V_p/V_s anomalies, arising from a lower V_p compared to V_s, dominate the geothermal field of Larderello-Travale. These have been interpreted as due to steam-bearing formations. On the contrary, analysis of $V_p \times V_s$ images provides information on the relative changes in rock porosity at depth. Comparison of tomographic section images with previously interpreted seismic lines suggests that the reflective '*K-horizon*' delineates a transition between zones that have different porosities or crack gatherings. The '*K-horizon*' also lies on low V_p/V_s anomalies, which suggests a steam saturation zone, despite the reduced porosity at this depth.

1. Introduction

The steam-dominated geothermal field of Larderello-Travale was used for the first commercial production of electricity, and which came online in 1913. Enel-Geothermal Production, the ENEL Unit involved in the development of geothermal resources, has drilled more than 200 wells in this area, down to maximum depths of about 4.0 km below sea level, in order to exploit the steam reservoirs. The whole geothermal area is about 400 km^2 and has a production of more than 1000 kg/s of super-heated steam, with a running capacity of about 700 MW (Cappetti and Ceppatelli, 2005).

Since this area has been under development for the generation of electric power, it has been the target of many geophysical studies (for review, see Minissale, 1991) that have highlighted the relatively shallow structure of the area (up to 4 km). Seismic reflection lines have contributed to investigations into the deeper structure of the field by showing the presence of a discontinuous reflector (between 3 and 8 km in depth), referred to as the '*K-horizon*' in the literature (Batini and Nicolich, 1985; Batini et al., 1978, 1985; Cameli et al., 2000; Brogi et al., 2003). More recently, three-dimensional (3D) seismic surveys have been carried out with a view to improving the location of deep drilling targets (Cappetti et al., 2005).

One of these deep structure investigations of the Larderello-Travale geothermal field has used high-resolution 3D tomographic inversion of microearthquake P-wave travel times (Vanorio et al., 2004). Results from this study have shown the presence of a deep high P-wave velocity structure. This structure follows the '*K-horizon*' with a convex shape that deepens towards the north-eastern and the south-eastern sides of the field. The '*K-horizon*' lies within the lower P-wave velocity zone, just above both the high-velocity structure and the earthquake locations. A reliable location of the earthquakes showed that the hypocentres thicken in a narrow zone between the '*K-horizon*' and the deep high-velocity structure revealed by P-wave velocity tomography. Together with geological and geophysical evidence collected by previous studies, these findings have led to the hypothesis that the '*K-horizon*', which lies just on the top of the high-velocity structure, represents the seismic signature of a fractured zone containing fluids under pressure.

* Corresponding author. Tel.: +39 0824323658; fax: +39 0824323623.
E-mail address: dematteis@unisannio.it (R. De Matteis).

0031-9201/$ – see front matter © 2008 Elsevier B.V. All rights reserved.
doi:10.1016/j.pepi.2008.04.019

Knowledge of the P-wave velocity field alone is not sufficient to be able to connect the velocity changes to deep variations in physical rock properties due to fluid content and porosity. To achieve this, the determination of reliable S-wave velocities and V_p/V_s and $V_p \times V_s$ models is crucial to differentiate cases that remain ambiguous using P-wave velocity information alone. For instance, Prasad (2002) and Dvorkin et al. (1999) have shown that the V_p/V_s ratio allows the differentiation of a low P-wave velocity due to overpressure or to the presence of gas. The present study has used the same dataset provided by Enel for the above-mentioned tomographic inversion (Vanorio et al., 2004), and it has been addressed to image a 3D S-wave velocity model of the Larderello-Travale field through a tomographic inversion of microearthquake S-wave travel times.

To improve the effectiveness of this interpretation, the sensitivities of the seismological parameters investigated have been estimated for site-relevant rocks under specific physical conditions. Theoretical rock physics signatures of these parameters have been computed by effective porous medium modelling (Dvorkin et al., 1999). This cross-disciplinary approach contributes to the study of the Larderello-Travale geothermal field by showing an imaging of the field in terms of the V_p/V_s ratio and $V_p \times V_s$ product, and the correlation of these to the reservoir rock physical properties, such as fluid content and porosity.

2. Geology and reservoir formations

The Larderello-Travale geothermal area is located on a structural high within the northern pre-Apennine belt (Fig. 1). During the late Miocene, this area experienced extensive tectonic activity that resulted in a block faulting structure, with horsts and grabens and a NW–SE trend. The anomalous heat flow that characterizes the Larderello area appears to be related to granitic stocks emplaced during the post-orogenic phase (Abbate et al., 1970; Puxeddu, 1984). At a few kilometres of depth, the temperatures that can be measured are more characteristic of medium to deep crust levels. Therefore, wells dug to 4-km depths have temperatures estimated at 450 °C at their bottom.

Fig. 2 illustrates the tectono-stratigraphic units of the area and their average velocities (Batini et al., 1978; Minissale, 1991; Brogi et al., 2003). The stratigraphic sequence consists of (1) post-orogenic sediments; (2) Ligurian units with embedded ophiolite blocks; (3) calcareous rocks (Tuscan Nappe); (4) evaporite units; (5) limestone, quartzite and phyllites (the Monticiano-Roccastrada Unit); (6) Methamorphic basement composed of phyllites and gneiss. Post-orogenic sediments and Ligurian units act as the cap-rock formations in the Larderello area (Minissale, 1991).

Energy production from geothermal sources in the Larderello-Travale field started at the beginning of the last century, firstly

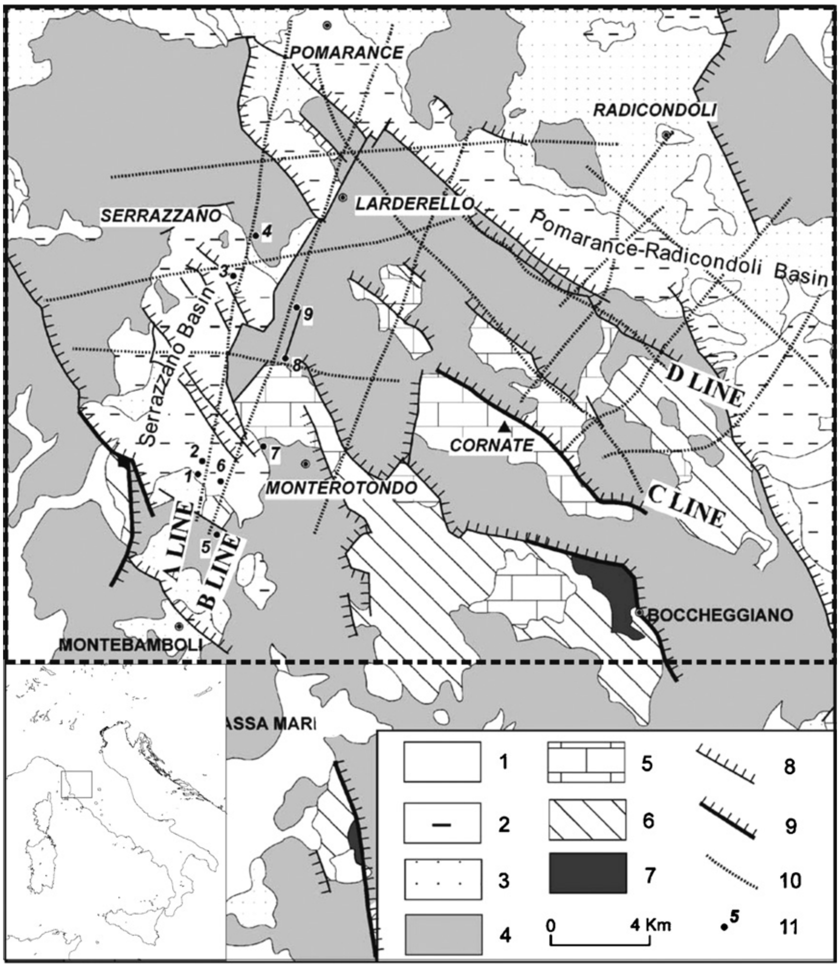

Fig. 1. Geological sketch map of the Larderello area. Inset, Italy and Tuscany map showing the target location. (1), (2), and (3) Cenozoic marine and continental sediments; (4) Ligurian Complex; (5) Tuscan Nappes: carbonatic sequence; (6) Tuscan Nappes: basal evaporites; (7) phyllites formation; (8) normal faults; (9) mineralized normal faults; (10) seismic lines; (11) borehole locations (modified from Brogi et al., 2003). Dotted box represents the area investigated in this study and showed in Fig. 3a.

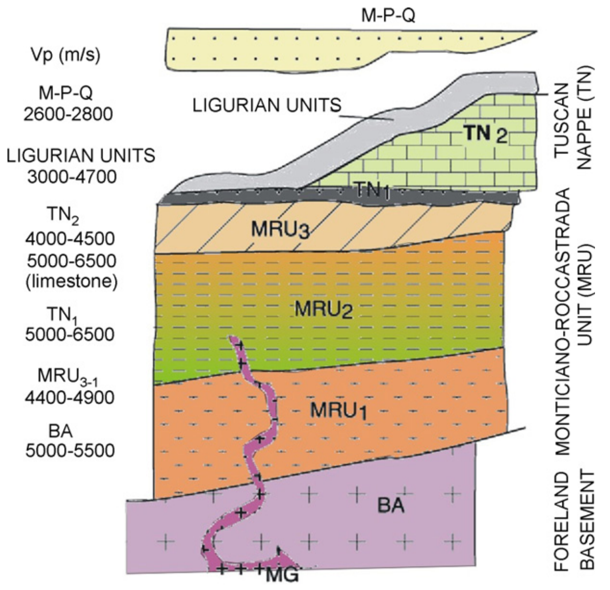

Fig. 2. Tectono-stratigraphic units outcropping in the Larderello area. MPQ, Cenozoic sediments; TN, Tuscan Nappes: TN2, carbonatic sequence, and TN1, basal evaporites; MRU, Monticiano-Roccastrada Unit: dolostones, limestones, and quartzites (MRU3), phyllites and quartzites (MRU2); micaschists (MRU1); BA, gneiss complex; MG, magmatic intrusion (modified from Brogi et al., 2003). The figure is a schematic representation of temporal sedimentary sequence and does not reproduce the real thickness of units. The average velocities of the formations are given on the left (Batini et al., 1978).

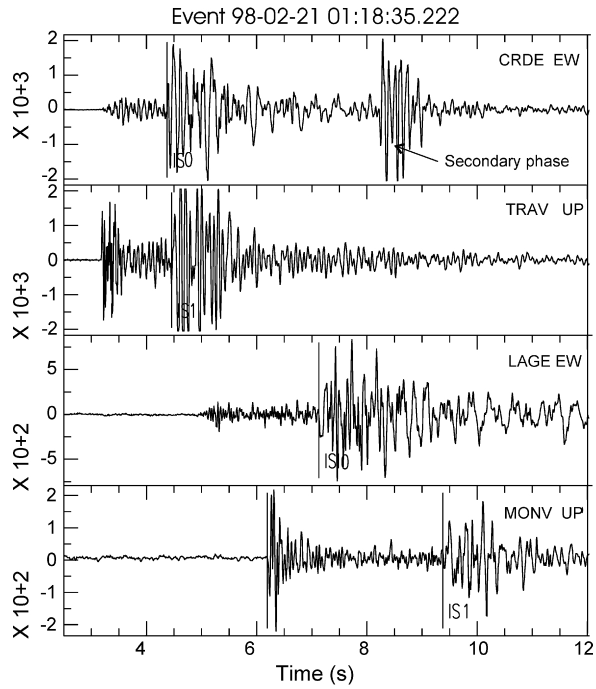

Fig. 4. Typical seismograms of the Larderello data set with the S first-arrival-times and relative weights are shown. Time readings have been weighted by a standard 0–4 coefficient related to the reading errors (weights of 0, 1, 2, 3 and 4 were associated, respectively, to uncertainties of ≤0.05, 0.05–0.10, 0.10–0.15, 0.15–0.20, and >0.20 s).

exploiting a high, fractured, super-heated steam reservoir located in the carbonatic–anhydritic formations. This shallower reservoir is located within the Tuscan Nappe and the upper part of the Monticiano-Roccastrada Unit, down to about 1 km in depth. It shows pressures and temperatures that range between 0.2 and 1.5 MPa and 150 to 260 °C, respectively (Cameli et al., 2000; Cappetti et al., 2000). At the beginning of the 1970s, the decline in production within the shallow reservoir forced the exploration towards a deeper one, located in the phyllite, micaschist, gneiss and granitic bodies down to 3–4 km in depth. At the same time, water reinjection into the shallow reservoir started as an exploitation strategy that was aimed at both sustaining the reservoir pressure and increasing the steam production. This deep reservoir is characterized by a pressure of about 7.0 MPa and temperatures

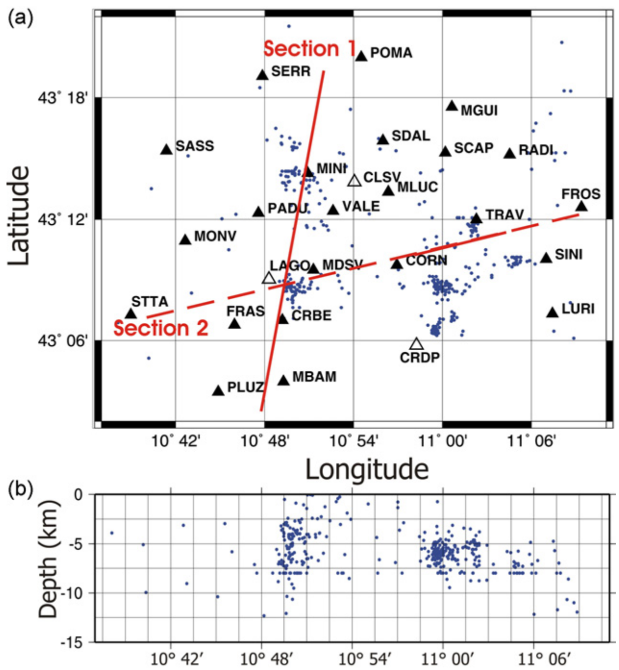

Fig. 3. (a) Map showing the seismic station locations (triangles) of the ENEL permanent recording network, and seismic event locations (dots) used in the present study. Casa la Serra (CLSV), Croce di Prata (CRDP) and Lago (LAGO) are the three stations with three-component sensors. (b) W–E section showing the depth of the hypocentres following a preliminary events location.

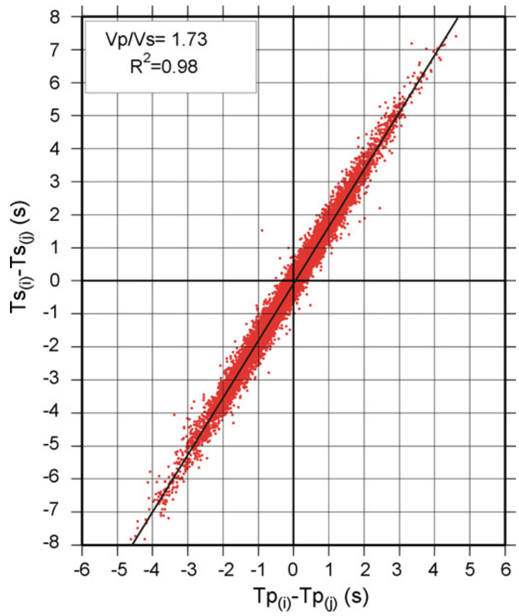

Fig. 5. $T_{si}-T_{sj}$ as function of $T_{pi}-T_{pj}$; the (i) and (j) indices refer to the recording stations. The pairs refer to P-wave and S-wave reading times weighted as <2 (uncertainty <0.1 s) and <3 (uncertainty <0.2 s), respectively.

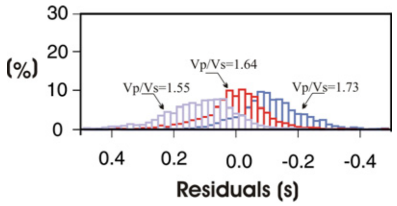

Fig. 6. Travel-time residuals calculated using S-wave velocity models obtained from different V_p/V_s values.

that range between 300 and 350 °C (Cappetti et al., 2000). The metamorphic basement and the overlying calcareous-anhydrite formations constitute a structural high that falls into a wide negative gravimetric anomaly. To reproduce this anomaly, 2D gravimetric models require the presence of low density bodies (2.45 g/cm^3), that have been interpreted as granite intrusions at depths ranging between 8 and 12 km (Barelli et al., 2000).

3. Travel-time tomography

The Larderello-Travale geothermal area is characterized by some hundreds of microearthquakes per year, with magnitude in the range of 0.0–3.0. Since 1977, the seismic activity has been recorded by a local digital network that has been altered over time due to the number and locations of the seismic stations. The network is composed of 26 short-period seismometers, of which only three have three-component sensors: Casa la Serra (CLSV), Croce di Prata (CRDP) and Lago (LAGO) (Fig. 3). The data used in the present study were digitized at 125 samples per second.

Epicentre locations are spread over the whole of this exploited region, even though clusters are seen in particular areas; the hypocentre depths are seen mainly down to 10 km in depth (Fig. 3). We have analyzed the same dataset that was used by Vanorio et al. (2004) to retrieve the 3D P-wave velocity structure of the Larderello-Travale field. The data consist of 500 microearthquakes that were recorded between January 1994 and September 2000, providing ∼7000 P-wave and ∼4000 S-wave first-arrival-time readings. Typical examples of seismograms of the Larderello data set with picked first S-wave arrival times are shown in Fig. 4. To retrieve a reliable P-wave and S-wave velocity models of the geothermal area, the P-wave and S-wave first-arrival-times need to be simultaneously inverted for both earthquake location and velocity model parameters. Since the P-wave and S-wave arrival-time readings have different qualities, both in terms of numbers and accuracy, we have preferred not to perform such a joint inversion, but have instead used the S-wave travel times independently.

3.1. Method

The tomographic inversion procedure used in this study follows the method described by Benz et al. (1996) that provides for velocity structure and earthquake location. It has been successful applied in several areas of the world (Okubo et al., 1997; Villasenor et al., 1998; Monna et al., 2003; Zollo et al., 2003). A finite-differences technique is used to compute the travel times, by solving the Eikonal equation through a complex velocity structure (Podvin and Lecomte, 1991) and the least squares LSQR algorithm (Paige and Saunders, 1982) for simultaneous inversion of the velocity structure and hypocentre parameters. The method uses smoothness constraint equations to regularize the solution controlling the

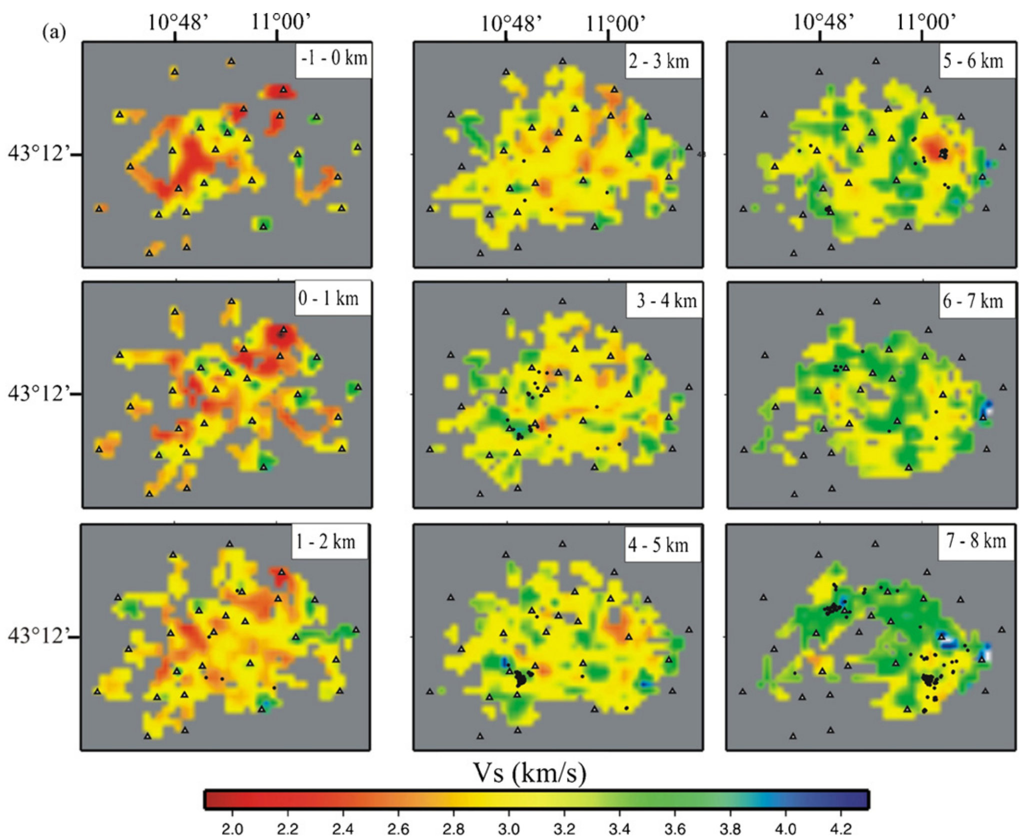

Fig. 7. (a) Map of the 3D S-wave velocity model from the surface down to 8 km in depth. The cells not covered by rays are in grey. (b) Map of the 3D P-wave velocity model obtained by Vanorio et al. (2004). (c) Plots of arrival-time residuals as a function of distance and residual histogram before (red) and after (blue) tomographic inversion runs for the S-wave velocity models.

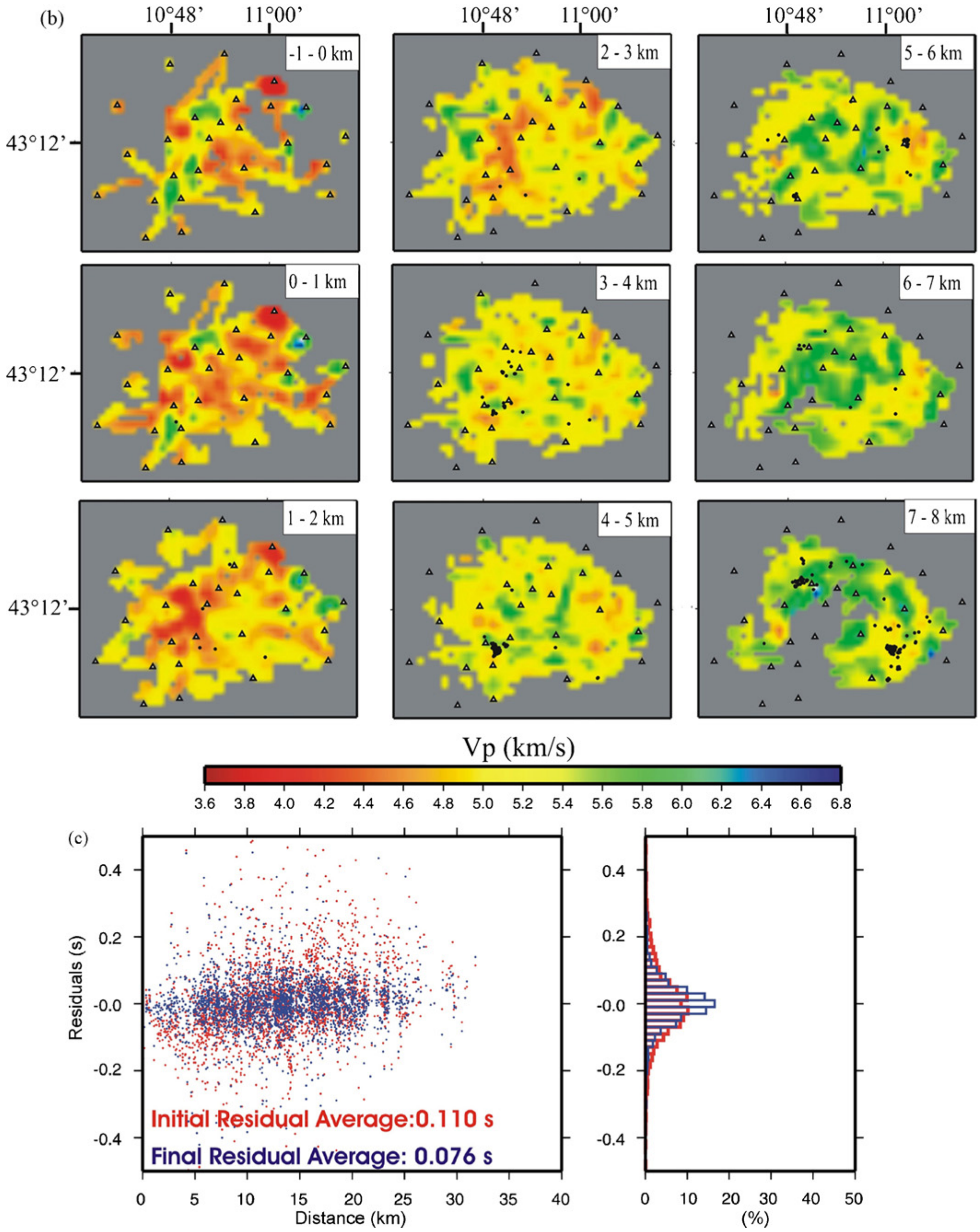

Fig. 7. (*Continued*).

velocity variation that is allowed during the inversion procedure in near cells. The approach proposed by Benz et al. (1996) solve for the S-wave model and the P-wave model independently, using an iterative, linearized approach. In our opinion, it is suitable for cases in which the ratio N_p/N_s (with N_p and N_s are the numbers of P and S time readings, respectively) is high and the uncertainty on the S-wave readings is larger than P uncertainty. In effect, the V_p model will be constrained by P data that are more numerous and of better quality, and the best V_s model will be searched by a local inversion method using the best V_p model as the reference model.

3.2. Data selection, starting model and model parameterization

From the initial data set, and as in Vanorio et al. (2004), we selected earthquakes with at least 10 phases read and characterized by weight ≤ 2 and ≤ 3 for the P-wave and S-wave arrival times, respectively, an azimuthal gap <180 degrees, and RMS residuals <0.5 s. The final dataset used for the inversion consisted of 400 well-located earthquakes, providing ~3000 S-phase first-arrival-times.

The best initial S-wave velocity model was derived from the 3D tomographic P-wave velocity model (Vanorio et al., 2004) by choosing an appropriate V_p/V_s ratio, as described below. For each event, P-wave and S-wave readings were selected to represent $(T_{s(i)}-T_{s(j)})$ as a function of $(T_{p(i)}-T_{p(j)})$-pairs, where the (i) and (j) indices refer to the recording stations (Fig. 5). Assuming a homogeneous half space, the data should fall along a straight line with a slope equal to the V_p/V_s ratio. The observed $(T_{p(i)}-T_{p(j)})$ and $(T_{s(i)}-T_{s(j)})$ arrival-time pairs were well distributed around a linear trend, where the least square best fit line provided a V_p/V_s of 1.73 ± 0.26 (Fig. 5). As demonstrated by Chatterjee et al. (1985), geothermal areas show extremely variable V_p/V_s ratios that besides their lithol-

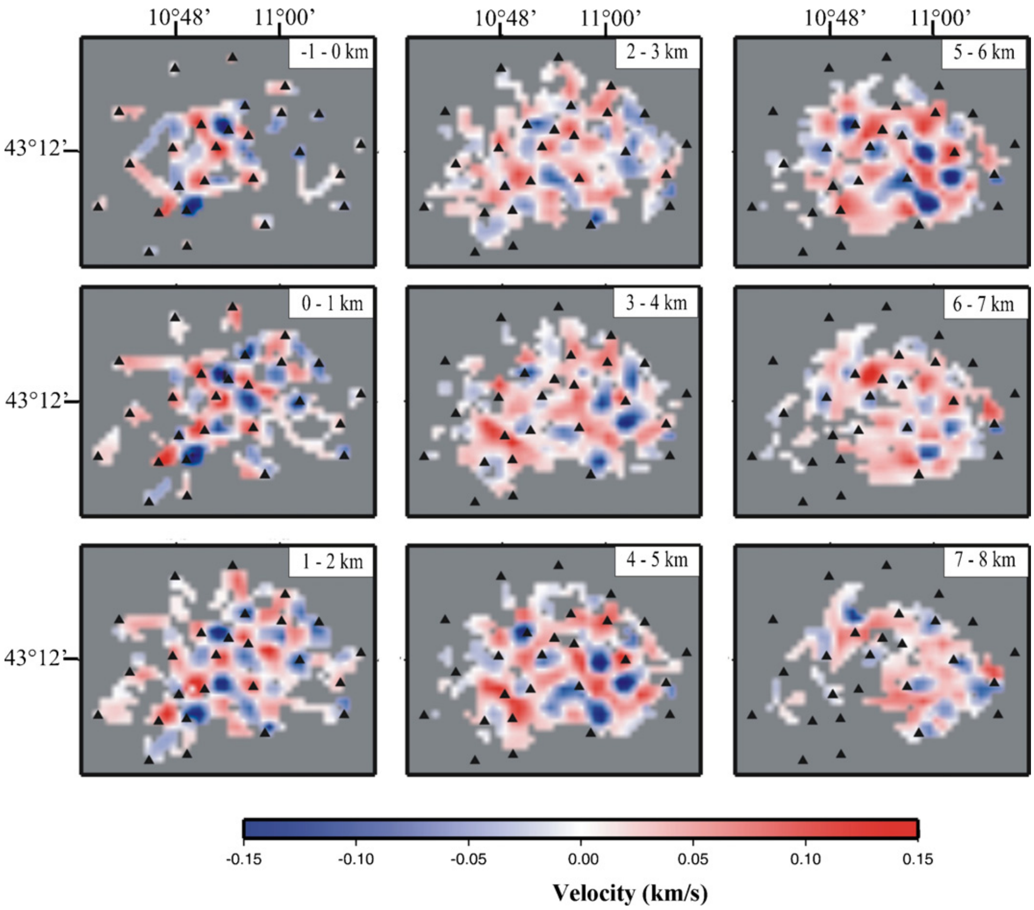

Fig. 8. Checkerboard tests for S-wave velocity model. Checkerboard cells from the input model are 2-km wide and correspond to a velocity anomaly of ±0.15 km/s.

ogy, is due to the presence of hot water at temperatures and pore pressures near the water-steam transition.

The travel-time residuals calculated for the S-wave velocity model derived from the P-wave model using a V_p/V_s value equal 1.73 are not well distributed around zero, as we would have expected. Several tests were performed to account for the variation in the range of V_p/V_s values shown in Fig. 5. The travel-time residuals illustrated in Fig. 6 that were obtained for three different values of V_p/V_s highlight that a V_p/V_s of 1.64 best minimizes the residuals of the initial V_s model, whereas values of 1.73 and 1.55 underestimate and overestimate them, respectively.

The distribution of the stations and events allowed the investigation of a volume of 46 km × 36 km × 16 km, with the top at 1 km above sea level. Trial inversions using different block sizes showed that the best model parameterization was a uniform horizontal and vertical grid spacing of 1 km with constant velocity cells. The grid spacing used to determine the 3D velocity model does not need to be the same as the grid spacing used to calculate arrival times. In fact, a smaller grid spacing of 0.5 km was used for accurate arrival-time calculations.

Table 1
Elastic moduli and densities of the phases used as the input parameters to generate the theoretical curves (Fig. 9)

Phases	K (GPa)	μ (GPa)	ρ (g/cm^3)
Quartz (40%) + calcite (60%)	57	36.7	2.69
Water (T = 200 °C, P_e = 30 MPa)	2.2	–	0.93
Steam (T = 400 °C, P_e = 30 MPa)	0.5	–	0.73

3.3. S-wave velocity structures

Fig. 7a shows a map of the 3D S-wave velocity structure from the surface down to 8 km in depth arising from this study. As a comparison, the map of the 3D P-velocity structure obtained by Vanorio et al. (2004) is also shown in Fig. 7b. Each layer is 1 km thick and the cells not crossed by any ray are shown in grey. After 20 iterations, the S-wave arrival-time residuals decreased by 31% from the initial arrival time RMS of 0.11 s. Fig. 7c shows the residuals before (red) and after (blue) the tomographic inversion runs for the S-wave velocity model. The histogram in Fig. 7c better highlights the decreases in the residual values from the initial (red) to the final (blue) values. The S-wave velocity spans a range of values between 1.8 km/s and 3.8 km/s, and shows similar patterns of P-velocity variation with depth. The retrieved P-velocity values are consistent with velocities used for the interpretation of seismic reflection lines (Batini et al., 1978; Brogi et al., 2003). Both the P-wave and S-wave maps show a localized low velocity zone beneath the Travale area at 5–6 km in depth.

Fig. 8 shows the spatial resolution of the retrieved S-wave velocity model through mapping the synthetic reconstruction of checkerboard velocity models. The synthetic S-wave arrival times were computed using the source-receiver geometry of our dataset and the retrieved S-wave velocity model perturbed by a checkerboard model. Different cell sizes have been tested; the most stable velocity models were provided by addition of a checkerboard model characterized by cells of 2 km × 2 km × 2 km and velocity of ±0.15 km/s. The results for the S-wave velocity model show that the velocity anomalies with wavelengths of the order of 2 km are

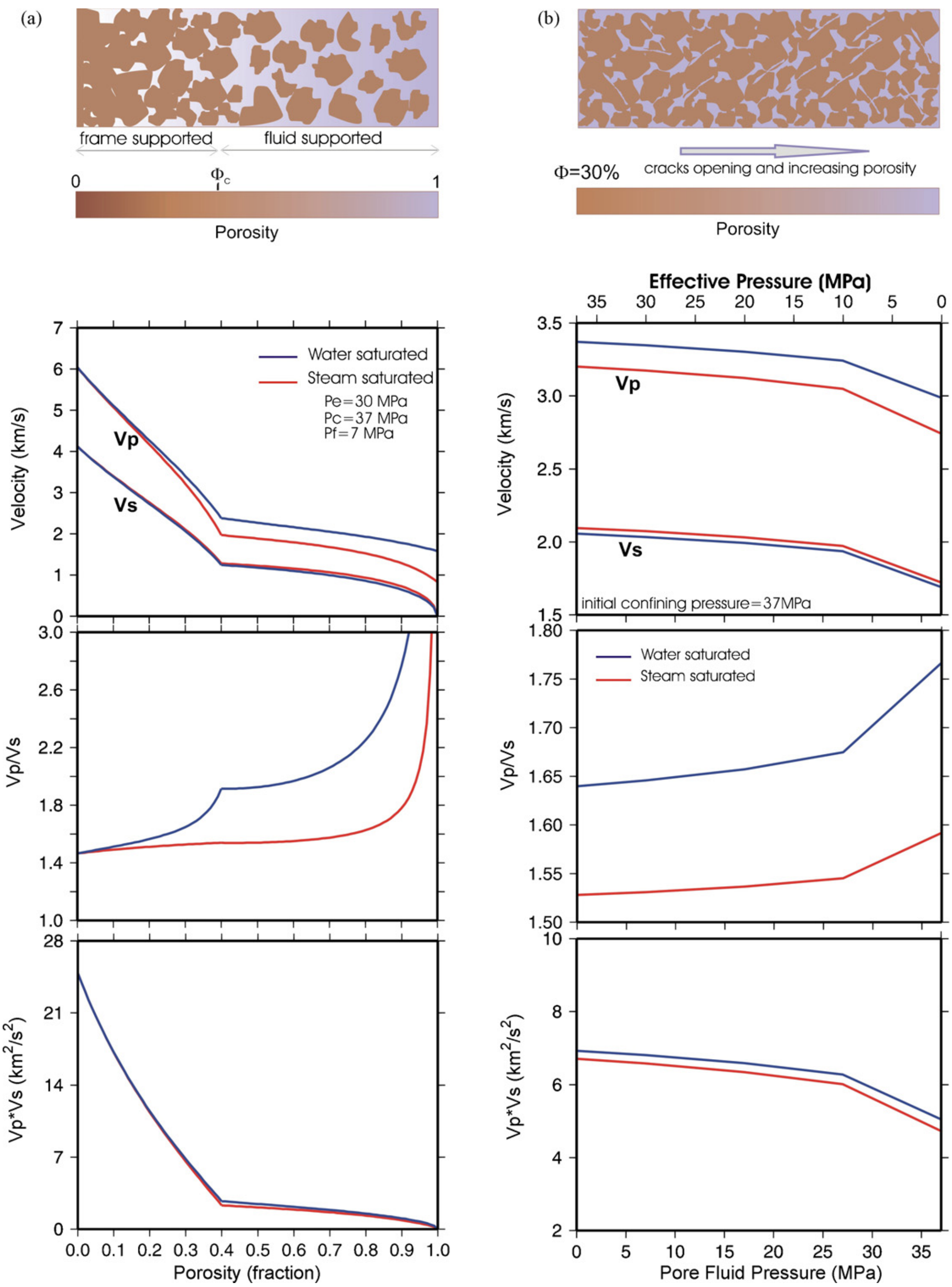

Fig. 9. (a) Theoretical computations of V_p and V_s as functions of porosity and saturating fluid (steam, red line; water, blue line) and derived curves for V_p/V_s and $V_p \times V_s$. (b) The variations in the parameters are calculated as a function of pore pressure. The elastic moduli and densities of the phases used as input parameters to generate these theoretical curves are given in Table 1.

reasonably well recovered in the central part of the volume investigated, up to 7–8 km. The resolution is poor at the edges of the model and at depths below 8 km, due to the lack of adequate ray coverage.

As most of the 4000 first S-arrival time readings are picked on the vertical component records, we have performed a Monte-Carlo experiment to estimate the stability of the inverse modelling using S data (Raffaele et al., 2006). We have perturbed the S-wave travel-times with random noise and repeated each time the inversion. The basic idea of this test is that if we increase the noise level, the results of the inversion should show an increased global misfit. If the global misfit remains about constant even for a large perturbation then this means that the model is not constrained by the observations. The noise level at which the global misfit starts to increase significantly from a constant behaviour is a statistical indicator of the error level on data. In our Monte-Carlo experiment, the

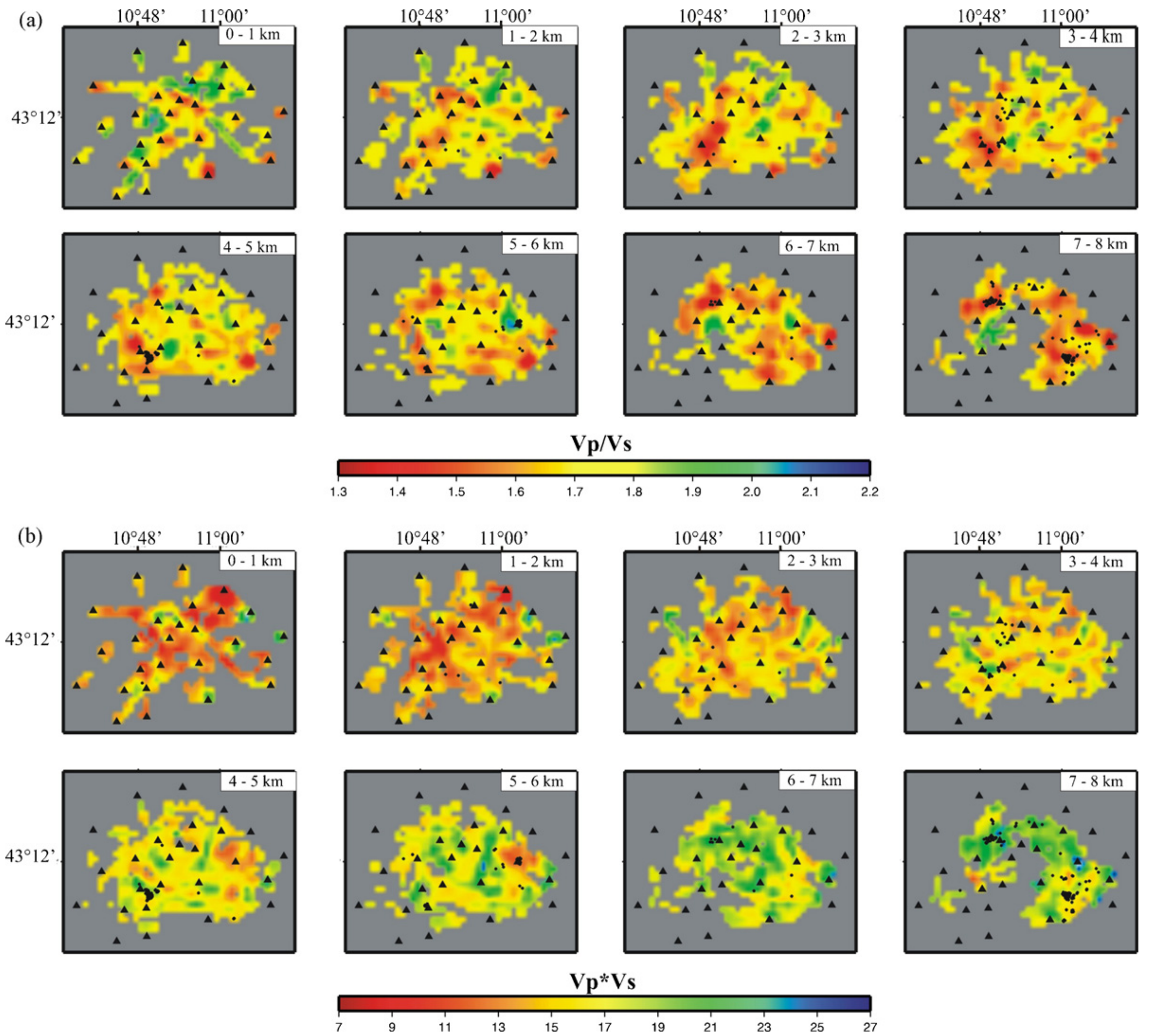

Fig. 10. Map of the 3D V_p/V_s (a) and $V_p \times V_s$ (b) structures and the earthquake locations from the surface down to 8 km in depth. The cells not covered by rays are grey.

noise level was varied from 0.05 to 0.3 s and for each level we have run the test several times. RMS remains almost constant with the noise level till a perturbation of about 0.2 s when it shows a sharp increase reaching a value 20% higher of the original RMS. Assuming the error on the S-wave readings to be equal to 0.2 s, we computed for this noise level the average deviations of the S-wave velocity for each cell of the model which are in the order of 0.1 km/s with the highest value equal to 0.15 km/s. These values represent the lowest amplitude threshold for velocity anomalies as detectable by S data, i.e. velocity differences in the tomographic images which are smaller than about 0.15 km/s are likely related to the uncertainty on arrival time picking.

4. Rock physics modelling

To interpret our seismological observations, it is advantageous to compare them either with theoretical results or with observations obtained during controlled experiments. Variations in seismic velocity depend on many physical conditions, so that linking them with observed seismological variations in tomographic images is quite difficult. However, since those conditions affect P-wave and S-wave velocities differently, cross-wise information of V_p and V_s and of the V_p/V_s ratio and $V_p \times V_s$ product help us to constrain the interpretation. In this section, we briefly review how the physical parameters affect seismic velocity, and then we report on rock physics modelling for site-relevant rock to emphasize how the comparisons between seismic parameters under different physical conditions allow the interpretation to be improved.

Mineralogy, cracks, saturation conditions, fluid characteristics, temperature and formation pressure all have roles in velocity variations (Birch, 1960; Spencer and Nur, 1976; O'Connell and Budiansky, 1974; Toksöz et al., 1976; Ito et al., 1979; Christensen, 1985; Christensen and Mooney, 1995; Sanders et al., 1995; Dvorkin et al., 1999). Since its mineralogy is an intrinsic property of the local rock, a significant correlation between lithology and observed V_p/V_s values has been suggested (Tatham, 1982); therefore, by rule of thumb, the lithology may be more fundamental than other factors that affect the velocity of rocks. However, the above-mentioned physical conditions often outweigh the reference lithology type, so that theoretical and experimental observations under different physical conditions constitute a further step in an understanding of the inferred velocity variation. O'Connell and Budiansky (1974) and Toksöz et al. (1976) showed that the presence of cracks and fractures decreases both V_p and V_s; since V_p decreases slower than V_s, V_p/V_s increases. Similarly, Dvorkin et al. (1999) numerically simulated the decreases in both V_p and V_s, and thus the increase in V_p/V_s, due to the opening of compliant thin cracks in the rock caused by pore pressure increases. Furthermore, if pores are saturated by fluids, V_p/V_s is much lower for gas saturation (e.g. high compressible fluids) than for liquid saturation (O'Connell and Budiansky, 1974; Ito et al., 1979). This observation derives from the concept that fluid compressibility governs the P-wave velocity variation, while the S-wave velocity remains nearly the same, driving the V_p/V_s changes. Finally, temperature influences the elastic properties of the rock, promoting in saturated rocks, fluid-phase transitions that affect the bulk modulus of fluids (Ito et al., 1979) as well as melting of rocks as the temperature approaches to near the *solidus*. Several theoretical and experimental studies (see Sanders et al., 1995 for review, and Murase and McBirney, 1973) have reported that most of the V_p and V_s changes (≈80–90%) occur in a narrow temperature range near the *solidus*. In this range, since V_s drops faster than V_p, the V_p/V_s ratio increases.

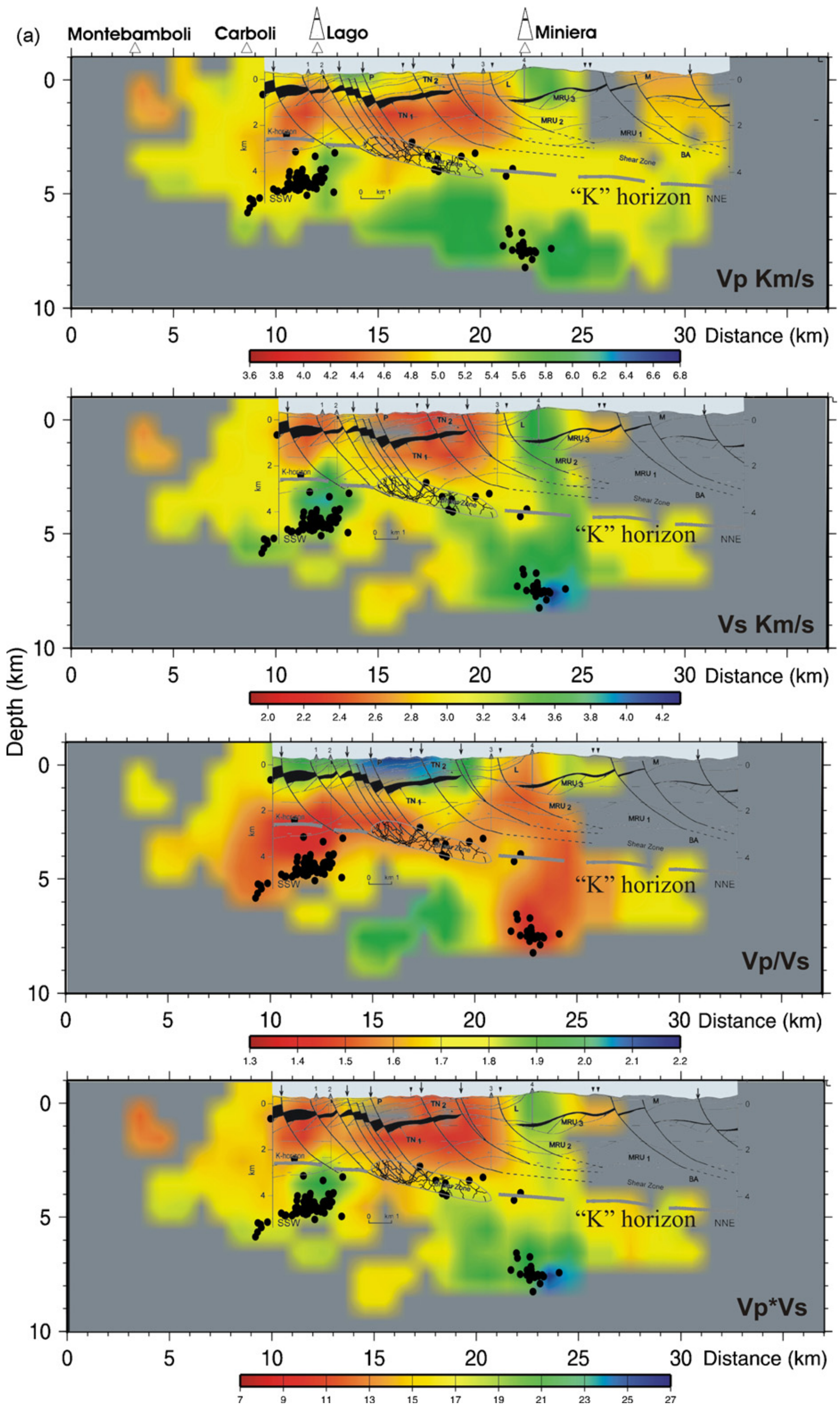

Fig. 11. Vertical cross-sections of V_p, V_s, V_p/V_s and $V_p \times V_s$. The orientations of the tomographic sections, Section 1 (a) and Section 2 (b), are shown in Fig. 3.

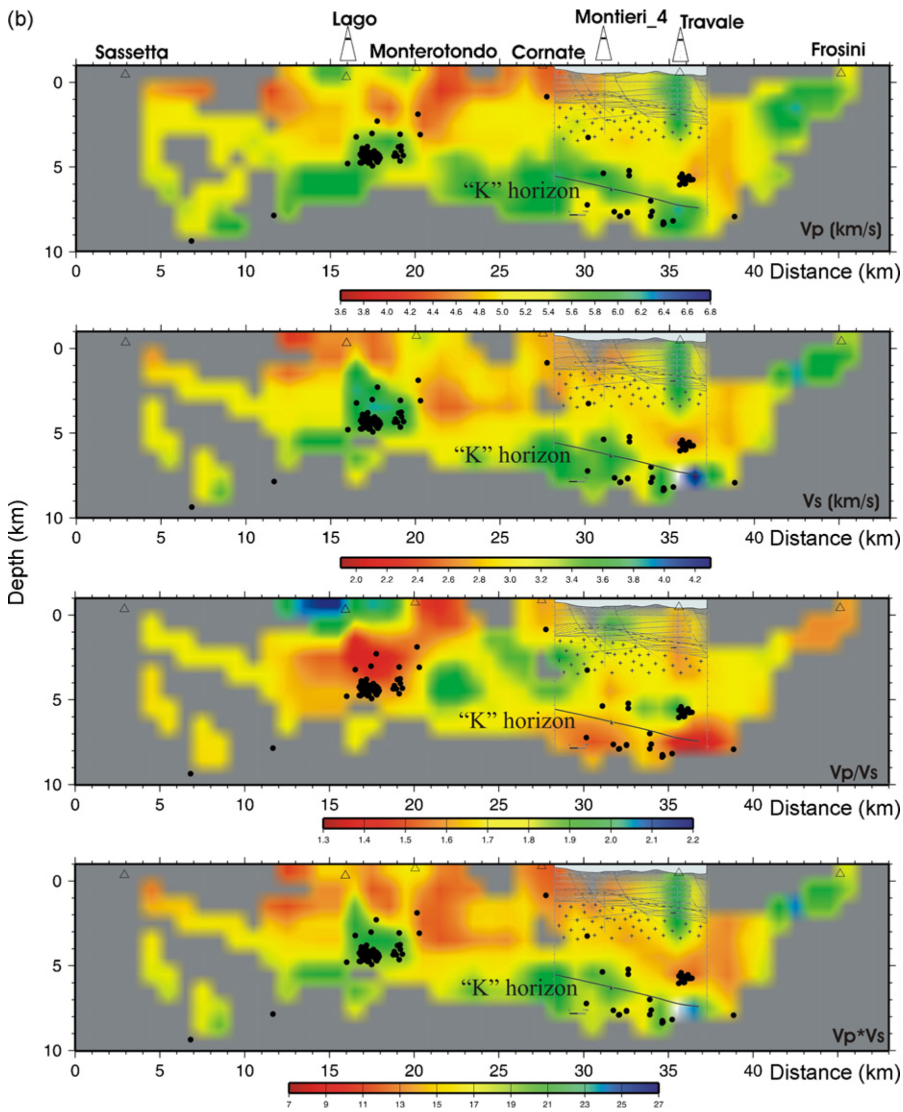

Fig. 11. (*Continued*).

Controlled laboratory experiments on site-relevant rocks are not available for the Larderello-Travale area. Nevertheless, to provide an estimate for the range of variation of the elastic parameters investigated, as well as for their sensitivities under specific physical conditions, we computed the seismic response of V_p, V_s, V_p/V_s and $V_p \times V_s$ as functions of saturation and porosity. We used the effective medium theory of Dvorkin et al. (1999) to compute theoretical rock P-wave and S-wave velocities as functions of porosity, pore fluid compressibility, mineralogy and effective pressure ($P_e = P_{confining} - P_{pore\ fluid}$). The modelling was performed under reservoir conditions of pressure and temperature, and concerns a fully steam- and water-saturated calcareous-quartzite rock, to best simulate the lithology of the area. Partial saturation (mixing of the two fluid phases) and patchy saturation have not been taken into account in this computation. The elastic input parameters used in the computation are shown in Table 1 (Mavko et al., 1998; Batzle and Wang, 1992); phase pressures and temperatures are also given.

As a first step, this model uses the Hertz-Mindlin (Mindlin, 1949) contact theory to compute the effective bulk (K_{HM}) and shear (μ_{HM}) modules of dry porous rock at critical porosity (Φ_c) under a given pressure (Nur et al., 1998). The critical porosity concept (Nur et al., 1998) separates the mechanical behaviour of a rock into two distinct domains. For $\Phi < \Phi_c$, the rock is frame supported and mineral grains are load bearing; on the contrary, for $\Phi > \Phi_c$, the rock simply 'falls apart', becoming a suspension in which the fluid becomes the load-bearing phase. In a second step, the variations in P-wave and S-wave velocities are calculated between the two end points at zero porosity (matrix point) (K_S and μ_S) and at the critical porosity (K_{HM} and μ_{HM}), as well as between the critical porosity (K_{HM} and μ_{HM}) and at 100% porosity (i.e. fluid point). Finally, the P-wave and S-wave velocities of the fluid-saturated rock are calculated using the Biot-Gasmann fluid substitution equations (see Dvorkin et al., 1999, for details).

Fig. 9a shows the theoretical computation of V_p and V_s as functions of porosity and saturating fluid (steam, red; water, blue). The derived values of V_p/V_s and $V_p \times V_s$ are also shown. Both V_p and V_s normally decrease with porosity. V_p values are higher for the water-saturated than for the steam-saturated rock, whereas V_s is not particularly sensitive to the nature of the saturating fluid. Note that the shear modulus of the rock is the same whether it is dry or saturated, so the only effect that pore fluids have on shear velocity is through increasing the density; this effect drives a decrease in V_s in water-saturated rock. It turns out that the departure of the derived V_p/V_s values from the matrix value depends on the fluid content: it is higher for water-saturated rock and lower for steam-saturated rock. Above the critical porosity, the rock behaves as a suspension and the elastic parameters approach those for the fluid phase. At the highest porosity, the S-wave velocity approaches zero and V_p/V_s increases. On the contrary, Fig. 9a shows that the change in $V_p \times V_s$ is less affected by fluid type and is instead more controlled by porosity along its entire range.

In the second modelling (Fig. 9b, top, right), the variations in the parameters are calculated as a function of pore pressure. The starting point is rock with a porosity of 30%. Increasing the pore pressure leads to an opening of cracks and an increase in porosity. The approach to the 'falling apart' condition (overpressure condition) determines the increase in V_p/V_s and the decrease in $V_p \times V_s$.

5. V_p/V_s and $V_p \times V_s$ images in the Larderello-Travale field

Images of the derived V_p/V_s ratio and $V_p \times V_s$ product are shown in Fig. 10. Porosity has been related to the velocity product $V_p \times V_s$ in both laboratory and *in situ* studies (Tatham, 1982; Iverson et al., 1989). However, due to a lack of rock property data for the lithology of the Larderello-Travale area, only the relative variation in $V_p \times V_s$ can be interpreted in terms of fluctuations in porosity.

Variation in these properties and their relations with P-wave and S-wave velocities can be seen in the sections reported in Fig. 11, which have been overlaid with the interpreted seismic lines (Brogi et al., 2003). Section 1 presented in Fig. 11a passes through the seismic stations Montebamboli (MBAM), Carboli (CRBE), Lago (LAGO), and Miniera (MINI) while Section 2 shown in Fig. 11b passes through Sassetta (SASS), Lago (LAGO), Monterotondo (MDSV), Cornate (CORN), Travale (TRAV), and Frosini (FROS). Low V_p/V_s anomalies dominate the geothermal field of Larderello-Travale. In particular, low V_p/V_s anomalies characterize the south-west part of the area, from 1 km down to 4 km in depth near the Lago, Carboli and Monterotondo zones. Deeper layers, between 6 and 8 km, show low V_p/V_s ratios near to the Miniera area. Since these anomalies derive from a lower V_p (i.e. a slight increase in V_p with depth) compared to V_s, they are interpreted as deriving from the presence of steam-bearing formations. The tomographic sections show that these anomalies mainly occur beneath the Lago and Miniera areas, down to 5 and 8 km in depth, respectively (Fig. 11a, Section 1a). On the contrary, higher and sparse V_p/V_s anomalies deriving from a higher V_p compared to V_s occur at shallow depths (e.g. the Lago area in the sections). These zones overlie the relatively lower V_p/V_s anomalies and might indicate either condensation zones where low pressure and higher porosity occur, or zones affected by water recharge. The analysis of the $V_p \times V_s$ image suggests that the reported '*K-horizon*' (Brogi et al., 2003) appears to delineate a transition zone towards formations with a relatively lower crack accumulation and/or porosity. Despite the reduced porosity at that depth, the low V_p/V_s anomalies still suggest steam saturation. This is based on the fact that even small amounts of gas are capable of greatly reducing P-wave velocity, driving V_p/V_s lower (Nur and Wang, 1989; Wang and Nur, 1992). Brogi et al. (2003) interpreted the K-reflector as representing the top of a brittle-ductile transition, where its reflectivity arises from the presence of overpressurized fluids. In the present study, we do not have evidence for a high V_p/V_s ratio indicating overpressure (Prasad, 2002; Dvorkin et al., 1999) along this zone. However, due to the inherent resolution of our images, the hypothesis of the presence of overpressurized fluids along the K-reflector cannot be ruled out. In fact, the only area that shows a well-constrained anomaly that accounts for an overpressure zone (i.e. low V_p, lower V_s, higher V_p/V_s, and low $V_p \times V_s$) occurs at 5–6 km beneath the Travale area (Fig. 11, Section 2).

6. Conclusions

High-resolution 3D S-wave velocity structures have been presented and used in the present study, along with the previously known 3D P-wave velocity model, to map the distributions of V_p/V_s and $V_p \times V_s$ in the Larderello-Travale geothermal field. Mapping of these last two derived parameters has been used to delineate zones at predominant steam saturation and at density fracture accruement, respectively. A comparison of these parameters with theoretical trends derived from effective porous medium modelling has been performed to interpret the results in terms of rock physics signatures.

Low V_p/V_s anomalies dominate the geothermal field of Larderello-Travale. Since these anomalies derive from a lower V_p compared to V_s, they are interpreted as steam-bearing formations. The Sections in Fig. 11 show that these anomalies occur at depth under the Lago and Miniera wells (see Section 1) and under the Lago-Monterotondo and Montieri-Travale zones (see Section 2).

Higher and sparse V_p/V_s anomalies (see Lago zone in Fig. 11a, Section 1) occur at shallow depths due to the higher V_p compared to V_s, and they are characterized by low $V_p \times V_s$. These zones might be related either to condensation zones or zones affected by water recharge.

A distinctive zone that occurs from 5–6 km under the Travale well (Fig. 11b, Section 2) is characterized by low V_p, lower V_s, higher V_p/V_s and low $V_p \times V_s$. An earthquake cluster is also seen at this depth. Cross-correlation of this information indicates the likelihood of an overpressured zone in which the higher porosity at this depth is supported by pore fluid pressure.

References

Abbate, E., Bortolotti, V., Passerini, P., Sagri, M., 1970. Introduction to the geology of the Northern Apennines in Development of the Northern Apennines geosyncline. Sedimen. Geol. 4, 207–642.

Barelli, A., Bertini, G., Buonasorte, G., Cappetti, G., Fiordelisi, A., 2000. Recent deep exploration results at the margins of the Larderello-Travale geothermal system. In: Proceedings 2000 World Geothermal Congress, Kyushu, Tohoku, Japan.

Batini, F., Burgassi, P.D., Cameli, G.M., Nicolich, R., Squarci, P., 1978. Contribution to the study of the deep lithospheric profiles: deep reflecting horizons in Larderello-Travale Geothermal field. Mem. Soc. Geol. Ital. 19, 477– 484.

Batini, F., Bertini, G., Giannelli, G., Pandeli, E., Puxeddu, M., Villa, I., 1985. Deep structure, age and evolution of the Larderello-Travale geothermal field. Geotherm. Res., Commun. Trans. 9, 253–259.

Batini, F., Nicolich, R., 1985. P and S reflection seismic profiling and well logging in the Travale geothermal field. Geothermics 14, 731–747.

Batzle, M., Wang, Z., 1992. Seismic properties of pore fluids. Geophysics 57, 1396–1408.

Benz, H.M., Chouet, B.A., Dawson, P.B., Lahr, J.C., Page, R.A., Hole, J.A., 1996. Three-dimensional P and S wave velocity structure of Redoubt Volcano, Alaska. J. Geophys. Res. 101, 8111–8128.

Birch, F., 1960. The velocity of compressional waves in rocks to 10 kilobars Part I. J. Geophys. Res. 65, 1083–1102.

Brogi, A., Lazzarotto, A., Liotta, D., Ranalli, G., 2003. Extensional shear zones as imaged by reflection seismic lines: the Larderello geothermal field (central Italy). Tectonophysics 363 (1/2), 127–139.

Cameli, G., Ceccarelli, A., Dini, I., Mazzotti, A., 2000. Contribution of the seismic reflection method to the location of Deep fractured levels in the geothermal fields of southern Tuscany (central Italy). In: Proceedings 2000 World Geothermal Congress, Kyushu, Tohoku, Japan.

Cappetti, G., Passaleva, G., Sabatelli, F., 2000. Italy country update report 1995–1999. In: Proceedings 2000 World Geothermal Congress, Kyushu, Tohoku, Japan.

Cappetti, G., Ceppatelli, L., 2005. Geothermal power generation in Italy: 2000–2004 update report. In: Proceedings 2005 World Geothermal Congress, Antalia, Turkey.

Cappetti, G., Fiordelisi, A., Casini, M., Ciuffi, S., Mazzotti, A., 2005. A new deep exploration program and preliminary results of a 3D seismic survey in the Larderello-Travale Geothermal field (Italy). In: Proceedings 2005 World Geothermal Congress, Antalia, Turkey.

Chatterjee, S.N., Pitt, A.M., Iyer, H.M., 1985. Vp/Vs ratios in the Yellowstone National Park region, Wyoming. J. Volc. Geoth. Res. 26 (3/4), 213–230.

Christensen, N.I., 1985. Measurements of dynamic properties of rocks at elevated temperatures and pressures. In: Pincus, H.J., Hoskins, E.R. (Eds.), Measurements of Rock Properties at Elevated Pressures and Temperatures. Spec. Tech. Publ.—ASTM, 869, 93–107.

Christensen, N.I., Mooney, W.D., 1995. Seismic velocity structure and composition of the continental crust: a global view. J. Geophys. Res. 100 (B6), 9761–9788.
Dvorkin, J., Prasad, M., Sakai, A., Lavoie, D., 1999. Elasticity of marine sediments: rock physics modeling. Geophys. Res. Lett. 26 (12), 1781–1784.
Ito, H., DeVilbiss, J., Nur, A., 1979. Compressional and shear waves in saturated rock during water-steam transition. J. Geophys. Res. 84, 4731–4735.
Iverson, W.P., Fahmy, B.A., Smithson, S.B., 1989. VpVs from mode-converted *P–S* reflections. Geophysics 54, 843–852.
Mavko, G., Mukerjy, T., Dvorkin, J., 1998. Rock Physics Handbook. Cambridge University Press.
Mindlin, R.D., 1949. Compliance of elastic bodies in contact. Trans. ASME 71, A-259.
Minissale, A., Aug 1991. The Larderello Geothermal Field: a review 1991. Earth-Sci. Rev. 31 (2), 133–151.
Monna, S., Filippi, L., Beranzoli, L., Favali, P., 2003. Rock properties of the upper-crust in Central Apennines (Italy) derived from high-resolution 3D tomography. Geophys. Res. Lett. 30, 7, doi:10.1029/2002GL016780.
Murase, T., McBirney, A.R., 1973. Properties of some common igneous rocks and their melts at high temperature. Bull. Geol. Soc. Am. 84, 3563–3592.
Nur, A., Mavko, G., Dvorkin, J., Galmudi, D., 1998. Critical porosity: a key to relating physical properties to porosity in rocks. The Leading Edge 17 (3), 357–362.
Nur, A., Wang, Z. (Eds.), 1989. Seismic and Acoustic Velocities in Reservoir Rocks: Experimental Studies, vol. 1. Society of Exploration Geophysicists, Tulsa, p. 405.
O'Connell, R.J., Budiansky, B., 1974. Seismic velocities in dry and saturated cracked solids. J. Geophys. Res. 79, 5412–5426.
Okubo, P.G., Benz, H.M., Chouet, B.A., 1997. Imaging the crustal magma sources beneath Mauna Loa and Kilauea volcanoes, Hawaii. Geology 25 (10), 867–870.
Paige, C.C., Saunders, M.A., 1982. LSQR: an algorithm for sparse linear equations and sparse least squares. ACM Trans. Math. Software 8, 43–71.
Podvin, P., Lecomte, I., 1991. Finite difference computation of traveltimes in very contrasted velocity models: a massively parallel approach and its associated tools. Geophys. J. Int. 105, 271–284.
Prasad, M., 2002. Acoustic measurements in sands at low effective pressure: overpressure detection in sands. Geophysics 67 (2), 405–412.
Puxeddu, M., 1984. Structure and late Cenozoic evolution of the upper lithosphere in Southwest Tuscany (Italy). Tectonophysics 101 (3/4), 357–382.
Raffaele, R., Langer, H., Gresta, S., Moia, F., 2006. Tomographic inversion of local earthquake data from the Gioia Tauro basin (south-western Calabria, Italy). Geophys. J. Int. 165, 167–179, doi:10.1111/j.1365-246X.2006.02872.x.
Sanders, C.O., Ponko, S.C., Nixon, L.D., Schwartz, E.A., 1995. Seismological evidence for magmatic and hydrothermal structure in Long Valley caldera from local earthquake attenuation and velocity tomography. J. Geophys. Res. 100, 8311–8326.
Spencer Jr., J.W., Nur, A.M., 1976. The effects of pressure, temperature, and pore water on velocities in Westerly Granite. J. Geophys. Res. 81 (5), 899–904.
Tatham, R.H., 1982. Vp/Vs and Lithology. In: Proceedings of the 50th Annual International Meeting, R35, Society of Exploration Geophysicists, pp. 2401–2414, Reprints.
Toksöz, M.N., Cheng, C.H., Timur, A., 1976. Velocities of seismic waves in porous rocks. Geophysics 41, 621–645.
Vanorio, T., De Matteis, R., Zollo, A., Batini, F., Fiordelisi, A., Ciulli, B., 2004. The deep structure of the Larderello-Travale geothermal field from 3D microearthquake traveltime tomography. Geophys. Res. Lett. 32, doi:10.1029/2004GL019432.
Villasenor, A., Benz, H.M., Filippi, L., De Luca, G., Scarpa, R., Patane, G., Vinciguerra, S., 1998. Three-dimensional P wave velocity structure of Mt. Etna, Italy. Geophys. Res. Lett. 25 (11), 1975–1978.
Wang, Z., Nur, A. (Eds.), 1992. Seismic and Acoustic Velocities in Reservoir Rocks: Theoretical and Model Studies, vol. 2. Society of Exploration Geophysicists, Tulsa, p. 457.
Zollo, A., Judenherc, S., Auger, E., D'Auria, L., Virieux, J., Capuano, P., Chiarabba, C., de Franco, R., Makris, J., Michelini, A., Musacchio, G., 2003. Evidence for the buried rim of Campi Flegrei caldera from 3D active seismic imaging. Geophys. Res. Lett. 30, 19, doi:10.1029/2003GL018173.